Cascaded Loop Control of a Three-Phase Grid-Connected PV Inverter System*

[1]A. B. Asiedu-Asante and [1]R. A. Ofosu
[1]University of Mines and Technology (UMaT), Tarkwa Ghana

Asiedu-Asante, A. B. and Ofosu, R. A. (2020), "Cascaded Loop Control of a Three-Phase Grid-Connected PV Inverter System", *Ghana Journal of Technology*, Vol. 5, No. 1, pp. 40 - 53.

Abstract

Owing to the advantages Photovoltaic (PV) systems possess over other renewable energy sources, more resources have been diverted into their advancement in recent years. These advantages combined with the increasing energy demand of the world have led to the commercialisation of PV power generation. One way of achieving large-scale utilisation of PV sources is through grid-connection. This paper focuses on the control of a three-phase grid connected PV inverter system that comprises a regulated boost DC-DC converter and a Heterojunction with Intrinsic Thin Layer (HIT) PV array. Perturb and Observe (P&O) Maximum Power Point Tracking (MPPT) Algorithm was used in the control of the boost converter and the Sanyo HIP-215NKHE5 solar module was chosen and simulated for system verification. For grid integration, a three-phase voltage source inverter was modelled together with an LCL filter. The inverter control used was a voltage-current cascade loop control scheme that employed Proportional Integral (PI) controllers in conjunction with a Phase Lock Loop (PLL) and the synchronous d-q frame control. The optimal PI gains were obtained using the Ziegler-Nichols method and the system was simulated in MATLAB/Simulink. With this control, the input to the inverter was maintained constant irrespective of the changing PV output voltage. The amount of current injected into the grid was regulated. The inverter system output was successfully synchronised with the grid in terms of phase and frequency, thereby improving power factor control. Though relatively not robust, this control strategy was relatively simple, easy to implement and efficient.

Keywords: Inverter, MPPT, PV, PI Controller, Cascade Control

1 Introduction

Industrialisation and population growth, have propelled the world energy demand on an upwards climb over the past years. This has influenced the demand for renewable energy sources such as photovoltaic (PV); making it more popular for sustainability with enormous potential. The role of power electronics and their associated control methodologies are critical for reliable and efficient operation of these PV systems.

A combination of the intermittent nature of PV output and low efficiency, typically ranging between 12 % to 29 %, necessitates the use of appropriate power converters to control and augment the generated power (Makhlouf *et al.*, 2012). Also, in order to convert the DC output of PV to grid suitable three-phase AC, a three-phase inverter is required. A number of control schemes are used to regulate these power electronics. They include artificial intelligent based control, conventional techniques such as proportional integral derivative (PID) control or a hybrid of control methods. Maximum power point tracking (MPPT) algorithms are also employed to ensure that the PV operates at the maximum power point (MPP) in any given climatic condition. The cascaded loop control combines the voltage and current control loops into a functioning closed loop. The controller utilized in this control loop may vary. The voltage control regulates power flow by controlling the phase angle between the grid voltage and the inverter output while the current control technique controls the active and reactive currents injected into the grid.

Over the years researchers utilize various types of controllers such as the Proportional Integral (PI) and PI-Derivative (PID) to control PV inverters. Truong and Tho, (2013) compared outputs from a PI based current regulator optimized by Particle Swarm (PSO), Genetic Algorithm (GA) and Ziegler-Nichols optimization techniques to determine the optimal PI gains. A fixed switching frequency was employed and the PSO provided the best results. Mooniarsih *et al.*, (2018) presented the concept of controlling the active and reactive power of a PV inverter output using an H-bridge topology DC-DC converter in conjunction with an inverter. The inverter control was implemented using pulse width modulation (PWM) and an auto-coupler pulse transformer. A PI compensator was used for DC voltage stabilization. Some works also considered the application of PI, Proportional Resonant Integral (PRI), Quasi-Proportional Resonance (QPR) control methods in single phase PV systems to mitigate harmonic distortion and improve system performance (Hannan *et al.*, 2015). Jia *et al.*, (2014) proposed the use of Proportional Resonant (PR) control together with Harmonic Compensator (HC) to minimize voltage disturbance in grid-connected PV inverter systems. The need for larger output filters of conventional controllers have encouraged works in the area of more

*Manuscript received February 24, 2020
Revised version accepted September 01, 2020

intelligent control techniques. Altin and Ozdemir, (2013), looked at a PV inverter system consisting of PI current regulator and a fuzzy logic based MPPT algorithm. Cespedes and Sun, (2014) also applied online grid impedance based adaptive control to a grid-connected PV inverter. An impulse-response analysis method was employed in the grid impedance measurement and Routh–Hurwitz stability analysis approach was then used in determining the stability boundaries of the interconnected system. Hannan *et al.* (2015) discussed the use of fuzzy logic based PWM PV inverter control for both stand alone and grid connected applications. The control method produced 2.48 % and 4.64 % voltage and current total harmonic distortions, respectively (Kammoun *et al.*, 2014)

This paper focuses on the performance of a simple PI controller-based control of a voltage source inverter using the cascade voltage and current loop control for automatic grid synchronisation and integration.

1.1 Overview of Grid Connected PV System

The system consists of a PV array connected to a MPPT controlled boost DC-DC converter. The DC-DC converter is in turn connected to a grid-tied inverter via a DC link capacitor as illustrated in Fig. 1.

The boost converter magnifies and controls the PV output to a ensure proper charging and stability of the DC link capacitor. The MPPT algorithm ensures that the panel is operating at its maximum power possible in any given climatic condition. This ensures that as much power as possible is extracted, for grid connection. With the output of the DC-DC converter being voltage, a PWM voltage source inverter is used. The cascade loop control is then applied to the inverter to facilitate automatic grid synchronisation.

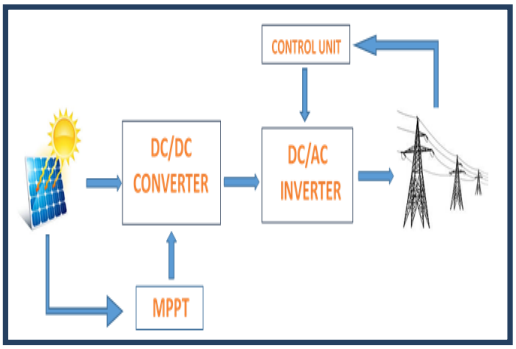

Fig.1 An Overview of Grid-Connected PV Inverter System

2 Resources and Methods Used

2.1 Modelling of PV Array

Considering the internal structure of the PV cell, the PV module was modelled mathematically, based on the Shockley diode equation and single diode structure of a PV cell (Makhlouf *et al.*, 2012 and Pandiarajan and Muthu, 2011). This model is of moderate complexity and consists of a DC current source in anti-parallel with a diode. The current source represents the photocurrent (I_L) generated from the sun and it is connected to series and parallel resistances, R_s and R_{sh} respectively as shown in Fig. 2. However, in this paper, the R_{sh} is assumed to be infinitely large and its effects are thus ignored. From Fig. 2, the net current generated (I_{pv}) is the difference of the photocurrent and the diode current (I_D) which is expanded as Equation (1).

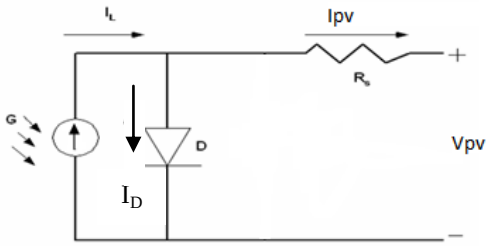

Fig. 2 Equivalent Circuit of a Solar Cell

$$I_{pv} = I_L - I_D = I_L - I_O\left[e^{\frac{q(V+I_{pv}Rs)}{nKT}} - 1\right] \quad (1)$$

Applying Shockley's diode equation, diode current is given as a relationship between output voltage (V) and generated current at non-illuminated conditions.

$$I_D = I_O\left[e^{\frac{q(V+I_{pv}Rs)}{nKT}} - 1\right] \quad (2)$$

Considering the diode saturation current (I_o) and its dependence on the temperature change gives Equation (3);

$$I_O = I_{O(Tr)} \times \left[\frac{T}{T_r}\right]^{\frac{3}{n}} \times e^{\left(\frac{-qV_g}{nK\left[\frac{1}{T}-\frac{1}{Tr}\right]}\right)} \quad (3)$$

Rated open-circuit voltage (V_{oc}) and short-circuit current (I_{sc}) were used to obtain the diode saturation current value at reference temperature ($I_{o(Tr)}$) as indicated in Equation (4).

$$I_{O(Tr)} = \frac{I_{sc(Tr)}}{\left(e^{\frac{qV_{oc}}{nKTr}-1}\right)} \quad (4)$$

Also, the model took into account the temperature dependence of the photocurrent in the Equations

(5) and (6). Equation (7) represented the dependence of the photocurrent on irradiance. With no current flowing through the diode at short-circuit, Equation (7) was set so as to generate the short-circuit current at the given irradiance (Gr).

$$I_L = I_{L(Tr)} + K_i(T - T_r) \quad (5)$$

$$K_i = \frac{I_{sc(T2)} - I_{sc(Tr)}}{(T_2 - T_r)} \quad (6)$$

$$I_{L(Tr)} = I_{sc} \times \frac{G}{G_r} \quad (7)$$

Again, the model, included the series resistance (R_s) which represented internal losses arising from current flow and cell connections within the module. According to Pandiarajan and Muthu (2011), experimentation with the I-V curve showed that R_s has a marked effect on the slope of the I-V curve at V = V_{oc}. Hence by differentiating and evaluating Equation (1) at V=V_{oc} and I = I_{sc} and rearranging in terms of R_s, Equation (8) was obtained. These were then evaluated at open-circuit conditions for initial value of series resistance.

$$R_s = -\left[\left.\frac{dv}{dI}\right|_{v_{oc}} - \frac{1}{X_v}\right] \quad (8)$$

Where;

$$X_v = I_{o(Tr)} \frac{q}{nKTr} e^{\frac{qV_{oc}}{nKT_r}} \quad (9)$$

K = Boltzman's constant = 1.3805×10^{-23} J/K,

q = electron charge=1.6×10^{-19} C

Vg = bandgap energy of semiconductor = 1.205 eV.

The Sanyo HIP-215NKHE5 PV module was modelled for this paper. This is a 215 W module with 72 HIT cells connected in series (Anon, 2009). Manufacturers specifications used in modelling are listed in Table 1. The diode quality factor (n) was initially set to 1.5 and adjusted to a more accurate value through curve fitting. The used array consisted of eight (8) modules connected in series to produce the output summarised in Table 2.

Table 1 Electrical Characteristics of the Sanyo HIP-215NKHE5 PV Module

Electrical Data	Value
Maximum Power, W	215
Max. Power Voltage, V	42
Max. Power Current, C	5.13
Open Circuit Voltage, V	51.6
Short Circuit Current, A	5.61
Temperature Coefficient of I_{sc}, A/ ^oC	0.00168
Number of Cells in Series	72
Standard Test Conditions (STC): Air mass 1.5, Irradiance 1000 W/m^2, Cell temperature 25 ^oC	

Due to the inclusion of the series resistance, Equation (1) became a recurrent equation, hence the Newton-Raphson iteration method was employed and final values of n = 2 and Rs = 4.4 mΩ provided the rated PV module characteristics as indicated by the manufacturer.

Table 2 Output Parameters of PV Array at 25 °C, 1000 W/m^2

PARAMETER	VALUE
Array Power, W	1720
Array Voltage, V	336
Array Current, A	5.13

2.3 Boost DC-DC Converter Modelling

The modelling process involved component selection and MATLAB simulation. Components were chosen based on the input values, desired output values, DC link capacitor rating, efficiency and operation of converter in continuous conduction mode (CCM) mode. With the output of the PV array being 1.72 kW, a converter of same power was modelled with an input range of 260 V to 360 V corresponding to the MPP between temperatures 0 ℃ -75 ℃.

2.3.1 Power Electronic Switch Selection

Based on the input voltage range from the PV array and the constant switching action of the MPPT, when incorporated, the Metal Oxide Semiconductor Field Effect Transistor (MOSFET) was used. The MOSFET is capable of handling current and voltage stresses up to 1 kA and 1.5 kV respectively, at a switching frequency greater than 1 MHz with very low losses.

2.3.2 Inductor Selection

Inductance value determine whether the converter operates in CCM or discontinuous conduction mode (DCM). From (Hasaneen and Mohammed, 2008), start-up time increases with increasing inductance value. Also, it enables higher current to be achieved at reduced ripple content. Smaller inductance values enable the inductor to charge up faster, reduce cost and power losses (Mohan *et al.*,1995). To ensure CCM mode, the inductance is selected such that inductor current flows continuously. Equation (10) determines the minimum inductance value at which the converter will be operating in the CCM-DCM boundary and also accounts for the current ripple content (Pattanaik *et al.*, 2016, Mohan *et al.*,1995 and Chan and Masri, 2010).

$$L_{min} = \frac{V_i \times (V_o - V_i)}{\Delta i \times F_S \times V_o} \quad (10)$$

The typical input voltage (V_i) of 336 V at STC, desired output voltage (V_o) of 500 V due to DC link voltage and switching frequency (F_S) of 20 kHz were used to evaluate the inductance value. According to (Das and Pradhan, 2011) the reasonable current ripple is about 20 % - 40 % of the current at MPP (I_{omax}). A 30% ripple content was assumed for this work as given in Equation (11) (Nandurkar and Rajeev, 2012).

$$\Delta i = 30\% \times I_{omax} \times \frac{V_o}{V_i} \quad (11)$$

I_o (1720 W / 500 V) was calculated to be 3.44 A and the ripple content 1.5 A. After substitution, the inductance value was calculated as 3.59 mH which was adjusted to 10 mH to reduce ripples further as this value also falls within the acceptable range of current ripple content.

2.3.3 Input Capacitor Selection

An input capacitor was required for connection with the PV array. This capacitor, according to (Nzar, 2014), ensured the converter peak current demands did not affect voltage supply. The minimum value was calculated using Equation (12) (Faisal, 2012).

$$C_{in} \geq \frac{I_m \times (D_m)^2}{0.02 \times (1 - D_m) \times V_{inm} \times F_s} \quad (12)$$

$I_m = I_o$ is the maximum current when the PV array is operating at MPP in STC. F_s is the switching frequency which is 20 kHz. D_m is the duty cycle at MPP. V_{inm} is the PV output voltage at MPP. The calculated value is 10.3 µF. Since Equation (12) provides a minimum value, the calculated value was then increased to 2 mF to reduce input voltage fluctuation.

2.3.4 Output Capacitor Selection

The capacitance, the equivalent series resistance (ESR) and desired voltage ripples were among the factors considered during selection. A low ESR offers better efficiency (Abdalrahman *et al.*, 2012). Equation (13) was used to calculate the minimum capacitance value of the output capacitor.

$$C_{out} \geq \frac{D \times V_o}{R \times \Delta V_o \times F_s} \quad (13)$$

From (Das and Pradhan, 2011), the allowable voltage ripple factor is 5% of output voltage according to International Electrotechnical Commission (IEC), which is 35 V in this case. Load resistance (R) was found to be 145 Ω at MPP and desired output voltage of 500 V. The calculated value was approximately 2 µF. This produced a high ripple in the resulting output voltage and was then adjusted to 2.5 mF. The boost converter operating parameters are summarised in Table 3.

Table 3 Boost Converter Parameters

Parameter	Operating Value
Input Power, W	1720
Input Voltage, V	336
Output Voltage, V	500
Duty cycle	0.35
Inductance, mH	10
Inductance Resistance, Ω	0.03
Capacitance, mF	2
ESR, Ω	0.001
Load Resistance, Ω	145

A Simulink model of the boost converter was developed as shown in Fig. 3.

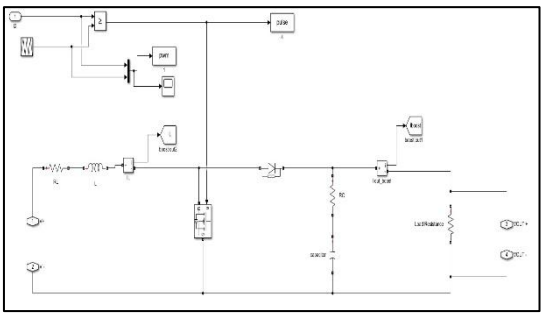

Fig. 3 The Simulink Model of the Boost DC-DC Converter

2.4 Maximum Power Point Tracking Algorithm

Power produced by solar cells varies with the operating voltage due to the cells non-linear behaviour (Makhlouf *et al.*, 2012). This implies that MPPT algorithms must track the voltage across the panel so as to ensure that it is operating at its MPP voltage. The MPP occurs at the knee of the P-V curve of a module for a given temperature and irradiance. The Perturb and Observe (P&O), algorithm was implemented together with the boost DC-DC converter. The choice is influenced by its simplicity and ease of design and its advantage of tracking slowing changing atmospheric conditions. The algorithm flowchart is shown in Fig. 4 where k is any sample point, V and P are the panel output voltage and power respectively and the D refers to the perturbation. The P&O algorithm was used to control the duty cycle of the boost converter. The algorithm was implemented in the MATLAB script file. The inputs of the function were the start-delay, voltage and current. The start-delay was implemented with a step input of magnitude 1 and the start time of 0.5. With this, the MPPT commenced operation after 0.5 seconds of the simulation time, allowing its operation to be well visualised. The input voltage and current were the

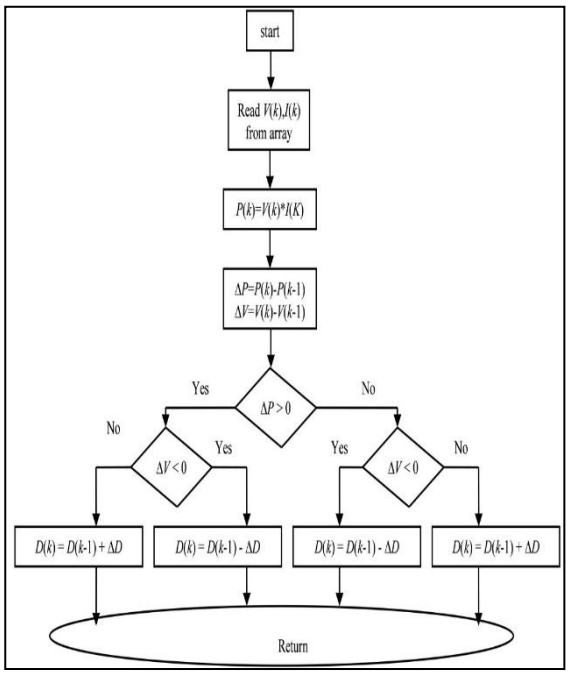

Fig. 4 Flowchart of the P& O Algorithm

panel voltage and current measured at the sample points.

Initial duty cycle (D_{init}) was set as 0.5 whiles the minimum (D_{min}) and maximum (D_{max}) duty cycles were 0.35 and 0.7 respectively. These were chosen to obtain the desired output voltage when operating between MPP voltage of 260 V at 75 ℃ and 360 V at 0 ℃. This range also accommodates the irradiance MPP voltage range between 100-200 W/m^2. The perturbation value (deltaD) was chosen to be 0.001. Variables V_{old}, D_{old} and P_{old} represent the previously sampled panel voltage, calculated power and duty cycle while V, D, P represent current samples. Initially, V_{old} and P_{old} are set to 0 whiles D is set to D_{init}. Following, the power is calculated at the sample point and compared with the previous power ($P\text{-}P_{old} = \Delta P$) and so is done for the voltage ($V\text{-}V_{old} = \Delta V$). Afterwards, the voltage perturbation is increased if both ΔP and ΔV were positive or negative ($\Delta P \times \Delta V > 0$). However, the perturbation was decreased if either ΔP or ΔV is positive or negative ($\Delta P \times \Delta V < 0$). To keep the duty cycle within range, a condition was added to maintain the current duty cycle if the value went above the D_{max} or D_{min}. Lastly, the current values were then stored as old values for the next iteration.

2.5 Inverter Modelling

The modelled inverter system consists of the three-phase voltage source inverter (VSI), its sinusoidal PWM (SPWM) switching scheme, an LCL filter and the two-loop cascade control technique for inverter operation and grid synchronisation as indicated in Fig. 5. The inverter system was modelled based on the grid parameters shown in Table 4. The three-phase VSI modelled consisted of six (6) MOSFET switches controlled by a bipolar PWM scheme. The inverter input is a relatively constant DC voltage source. The input to the PWM is the output of the cascade control unit, this is the demand voltage waveforms produced by the PI controllers from the generated error signal. This is then compared with a 5 kHz triangular waveform using the relational operation. A NOT gate is used to produce the negative half pulses of the control signal used for bipolar switching. The desired output voltage' s fundamental frequency (f_1) is same as the frequency of the control signal and its relationship with the inverter switching frequency (f_s) is given in Equation (14). Equation (15) also defines the ratio between the peak of the control voltage to the peak of the triangular waveform known as amplitude modulation (m_a) (Mohan *et al.,* 1995).

Table 4 Inverter System Design Parameters

Parameter	Value
Grid Line Voltage ($V_{L\text{-}L,\ rms}$)	415 V
Grid Phase Voltage ($V_{ph,\ rms}$)	240 V
DC link Voltage	500 V
Maximum power output	1720 W
Grid frequency	50 Hz
Inverter Frequency	20 kHz

$$\text{Frequency modulation } (m_f) = \frac{f_s}{f_1} \qquad (14)$$

$$m_a = \frac{V_{peak,control}}{V_{peak,tri}} \qquad (15)$$

The magnitude of the triangular waveform is determined using Equation (15). Assuming an amplitude modulation of 0.9, this was calculated to be 378 V DC.

2.5.1 Link Capacitor Calculation

With the output of the inverter being AC, the RMS values are defined for averages, however, the DC link voltage and capacitor are usually chosen to be large enough to support the peak values. From Table 4, the 240 V_{rms} phase voltage will have a peak of 340 V and hence the dc link capacitor is calculated to have a value to 500 V to accommodate for losses in the system. Equation (16) is used to determine the capacitance value for the dc link capacitor (Pattanaik, *et al.,* 2016).

$$C_{DC} = \frac{2 \times P_{max}}{f \times {V_{dc}}^2 \times (1 - k^2)} \qquad (16)$$

With the maximum power (P_{max}) being the system maximum power of 1.72 kW, grid frequency (f) of

50 Hz, the dc link voltage (V_{dc}) of 500 V and the constant k being equal to V_{dcmin}/V_{dc} = 400/500 = 0.8, the dc link capacitor was found to be 500 µF. This value was later adjusted to 1 mF to compensate for the increased boost converter inductance and to better sustain the boost converter output voltage.

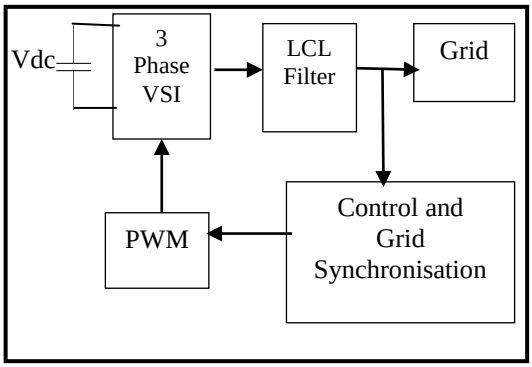

Fig. 5 Overview of the Grid-Connected Inverter System

2.5.2 LCL Filter Modelling

The component selection was based on Equations (17) – (20). The inverter side inductance (Li) was designed to limit the output current ripple by 10 %.

$$L_i = \frac{V_{dc}}{16 \times f_s \times \Delta I_L} \quad (17)$$

Where $\Delta I_L = 0.1 \times \frac{P_{in}\sqrt{2}}{V_{grid}}$ and P_{in} is the inverter power and V_{grid} refers to the grid voltage and fs the grid frequency. According (Abdalrahman, *et al.*, 2012), the filter must operate with a 5 % maximal power factor variation. The capacitance is thus determined by;

$$C_f = 5\% \left[\frac{1}{2\pi f_s \times \left(\frac{V_{grid}{}^2}{Pin} \right)} \right] \quad (18)$$

The grid side inductance (L_g) is calculated as a function of the inverter side inductance as expressed in Equation (19). In this equation, r is the calculating factor as used by Abdalrahman *et al.*, (2012) and the value was set as 0.6.

$$L_g = r \times L_i \quad (19)$$

To mitigate oscillations associated with the LCL filter, a passive damper was designed based on resonant frequency. The damping resistance (R_d) value is given as Equation (20).

$$R_d = \frac{1}{3 \times \omega_{res} \times C_f} \quad (20)$$

Where ω_{res} is the resonant frequency of filter is given by Equation (21).

$$\omega_{res} = \frac{1}{2\pi} \left[\sqrt{\frac{L_i + L_g}{L_i \times L_g \times C_f}} \right] \quad (21)$$

The values used were L_i = 9 mH, C_f = 6.7 µF, L_g = 5 mH and Rd = 7 Ω.

2.6 Inverter Control

The control strategy consists of two loops and it also employs the synchronous d-q reference frame control. The inner of the two loops is a current loop. This loop is faster, and it controls the power quality, total harmonic distortion (THD) and the current injected into grid. The outer loop on the other hand, is a voltage control loop that aims to stabilise the DC link voltage and balances the power flow in the system. Also, the control strategy employs proportional Integral (PI) controllers in each loop. A phase lock loop (PLL) is also included to accurately calculate the grid frequency and phase. The overview of the control system is illustrated in Fig. 6.

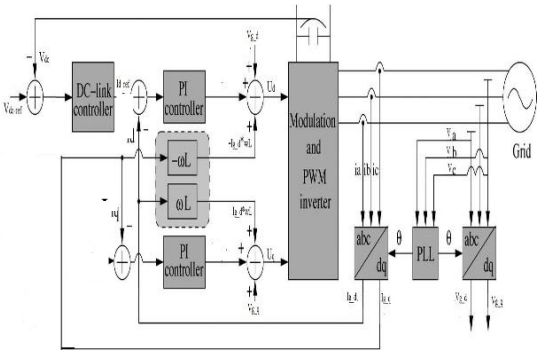

Fig. 6 Block Diagram of Inverter Control System

In the PLL and d-q transformation stage, the three-phase grid current (I_{g_abc}) and voltage (V_{g_abc}) are sensed and first transformed from three-phase to equivalent two-phase using Clark's transformation as expressed in Equations (22) and (23) respectively. The PLL determines the grid frequency (F_g) and phase angle (Θ) using the sensed three-phase grid voltage. The phase angle is then used to transform the two-phase currents (I_{g_a} and I_{g_b}) and voltages (V_{g_a} and V_{g_b}) from the stationary reference frame to the rotating reference frame producing currents (I_{g_d} and I_{g_q}) and voltages (V_{g_d} and V_{g_q}) respectively using Park transformation in Equations (24) and (25).

$$\begin{bmatrix} Ig\_a \\ Ig\_b \end{bmatrix} = {}^{2}/_{3} \begin{bmatrix} 1 & {}^{-1}/_{2} & {}^{-1}/_{2} \\ 0 & {}^{\sqrt{3}}/_{2} & {}^{-\sqrt{3}}/_{2} \end{bmatrix} \begin{bmatrix} Ig\_a \\ Ig\_b \\ Ig\_c \end{bmatrix} \quad (22)$$

$$\begin{bmatrix} Vg\_a \\ Vg\_b \end{bmatrix} = {}^{2}/_{3} \begin{bmatrix} 1 & {}^{-1}/_{2} & {}^{-1}/_{2} \\ 0 & {}^{\sqrt{3}}/_{2} & {}^{-\sqrt{3}}/_{2} \end{bmatrix} \begin{bmatrix} Vg\_a \\ Vg\_b \\ Vg\_c \end{bmatrix} \quad (23)$$

$$\begin{bmatrix} Ig\_d \\ Ig\_q \end{bmatrix} = \begin{bmatrix} \cos\theta & \sin\theta \\ -\sin\theta & \cos\theta \end{bmatrix} \begin{bmatrix} Ig\_a \\ Ig\_b \end{bmatrix} \quad (24)$$

$$\begin{bmatrix} Vg\_d \\ Vg\_q \end{bmatrix} = \begin{bmatrix} \cos\theta & \sin\theta \\ -\sin\theta & \cos\theta \end{bmatrix} \begin{bmatrix} Vg\_a \\ Vg\_b \end{bmatrix} \quad (25)$$

Fig. 7 shows a block diagram of typical PLL. The sensed grid voltage is transformed to d-q frame and the PLL locks phases at zero by setting the reference V_d to zero. The Voltage-Controlled Oscillator (VCO) is also an integrator that translates the PI output of frequency into phase angle. The grid and inverter voltages are synchronised when the phase angle difference becomes zero and $V_d = 0$ and V_q is the grid voltage. The Simulink model of the PLL with synchronous frame transformations is shown in Fig. 8. Considering the current control stage, the d-q currents generated (I_{g_d} and I_{g_q}) are then compared with the reference active and reactive currents (I_{d_demand} and I_{q_demand}) to determine the current error. These errors are fed to the PI controllers to produce corresponding signals to keep the error value minimal. The active current reference (I_{d_demand}) is obtained from the DC link voltage (V_{dc}) via the voltage control loop whiles the reactive current reference is set to zero. This is so because desired reactive power is zero. To find the voltage demand, Equation (26) is employed.

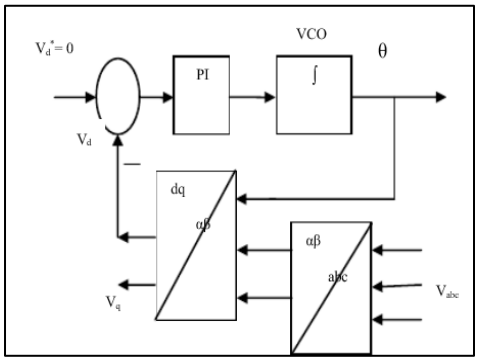

Fig. 7 PLL Block Diagram

$$\begin{bmatrix} U_d \\ U_q \end{bmatrix} = L\frac{d}{dt}\begin{bmatrix} i_d \\ i_q \end{bmatrix} + R\begin{bmatrix} i_d \\ i_q \end{bmatrix} + \omega L\begin{bmatrix} -i_q \\ i_d \end{bmatrix} + \begin{bmatrix} e_d \\ e_q \end{bmatrix} \quad (26)$$

Where R is the resistance between the grid and the inverter, ω is the grid angular frequency and L is the inductance between inverter and grid and together, ωL, is the decoupling factor. The resulting demand voltages (U_{dq}) serve as the d-q control signals which are transformed back into three phase stationary frame control signals (U_{abc}) using the inverse of Equations (23) and (25). The resulting signal then serve as the control signals for the inverter PWM.

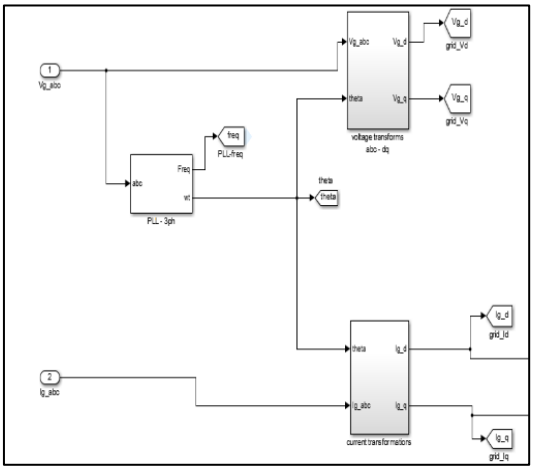

Fig. 8 Simulink Model of PLL with Synchronous Frame Transformations

The current control loop consists of the current PI controller, the inverter and the grid as shown in Fig. 9, where I_d^* is I_{dq_demand} and I_d is I_{g_d}. The figure shows the inner control loop with the major component expressed as transfer functions in s-domain. The MATLAB implementation is shown in Fig 10. The plant represents the inductance and resistive loads experience by the inverter including the inverter filter. Inputs to the loop are the reference and measured currents (I_{dq_demand} and I_{g_dq} respectively). These are obtained after the operation of the PLL.

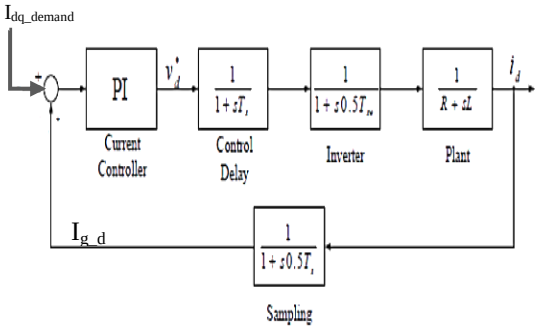

Fig. 9 Block Diagram of Current Control Loop

In the outer voltage control, the measured DC link voltage is compared with the reference voltage (500 V), the resulting error is fed to the voltage PI controller and a demand or reference active current is produced for use by the inner control loop.

The voltage control loop designed mainly consisted of the DC link voltage measurement, the voltage PI controller and the inner current loop as shown in Fig. 11. The inner current loop is represented by it transfer function and the load (plant) is mainly the DC link capacitor. Fig. 12 also illustrates the Simulink model of the entire control strategy. The proportional and integral gains of the current controller were obtained using the Ziegler-Nichols method to be K_p = 0.030 and K_i = 0.015 respectively. For the voltage controller, the gains were K_p = 2.214 and K_i = 2.32.

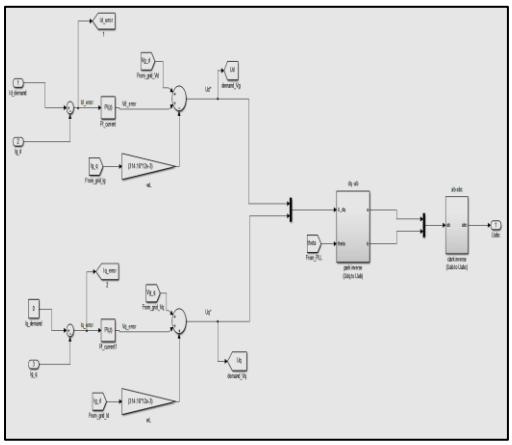

Fig. 10 Simulink Model of the Current Control Loop

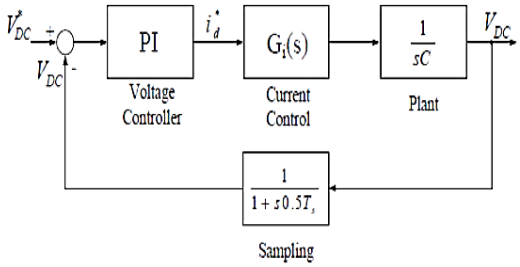

Fig. 11 Block Diagram of the Voltage Control Loop

3 Results and Discussion

Firstly, the individual components of the grid-connected inverter system were tested in close-to-ideal conditions to confirm their operation before system integration. Fig. 13 shows the current-voltage (I-V) curve of the simulated SANYO-HIP-215NKHE5 solar panel at STC indicating that open-circuit voltage V_{oc}= 51.6 V occurs at I= 0 A whiles short-circuit current I = 5.61 A occurs at V= 0. These match the values on the panel datasheet. Again, the maximum power point of the panel occurs at 42 V and 5.13 A corresponding to the manufacturer's ratings. From the power-voltage (P-V) curve shown in Fig. 14 the maximum power of the panel is 215.2 W at a voltage of 42 V which is quite close to the rated 215 W at same voltage.

With the 8 modules connected in series, the output I-V and P-V characteristics of the resulting array is shown in Fig. 15 and 16 respectively. All PV characteristics were simulated at irradiance (G) = 1000 W/m^2, temperature (T) = 25 ^{0}C.

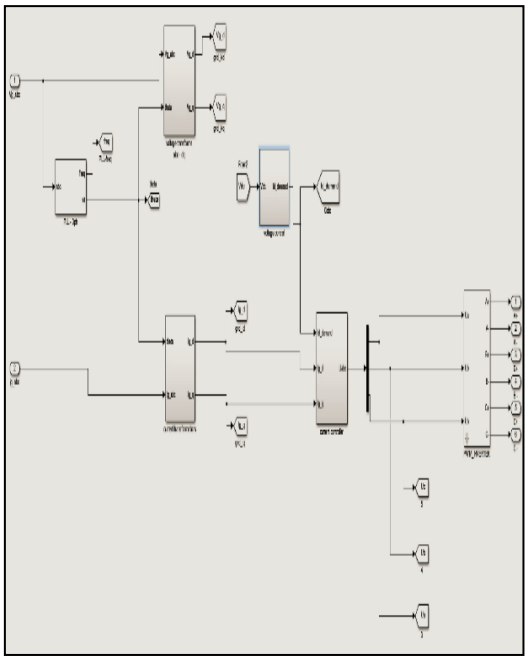

Fig. 12 Simulink Model of the Inverter Control

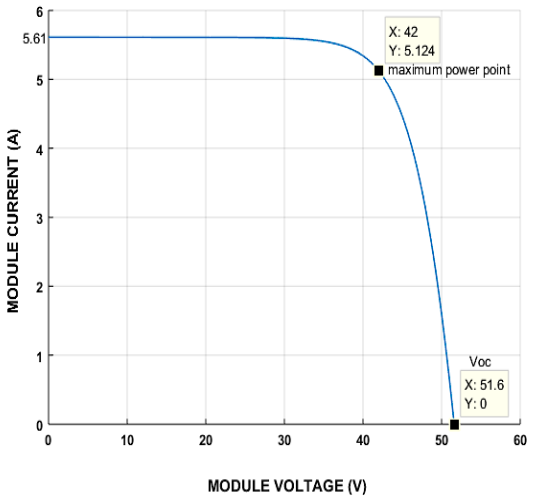

Fig. 13 I-V Characteristic Curve of PV Module

Fig. 15 and 16 display the array voltage and current values to be 336 V and 5.13 A respectively. These were achieved by increasing values of open circuit voltage, number of series connected cells and the series resistance per cell. Hence they reflect the number of cells connected to attain the array used.

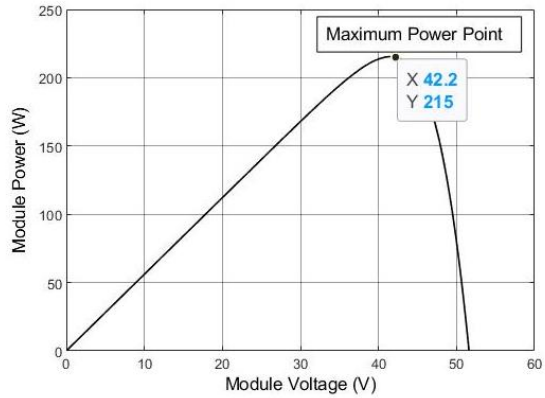

Fig. 14 P-V Characteristic Curve of PV Module

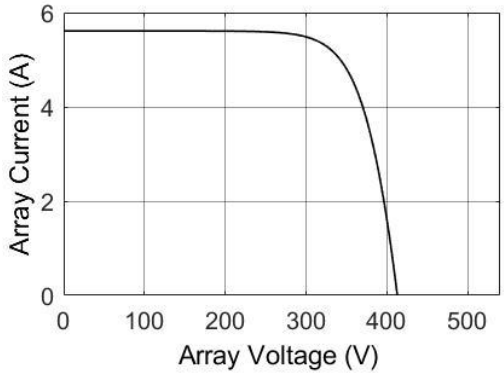

Fig. 15 I-V Characteristic Curve of PV Array

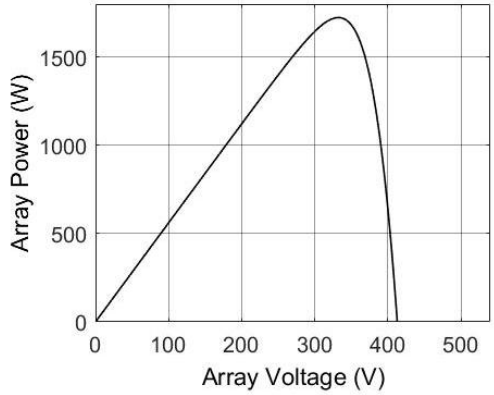

Fig. 16 P-V Characteristic Curve of PV Panel

In the Simulink environment, a discrete sampling time of 6 ms was used. The boost converter is assumed to be operating at nominal operating conditions (NOC) which gives the input values according to Table 3 and determine the duty cycle. In Fig. 17, the input voltage is shown to 336 V whiles the output voltage is 500 V instead of the calculated 516 V at that duty cycle. This loss in voltage is attributed to the internal losses in the converter arising from diode voltage drop, and inductive resistances as wells as switching losses.

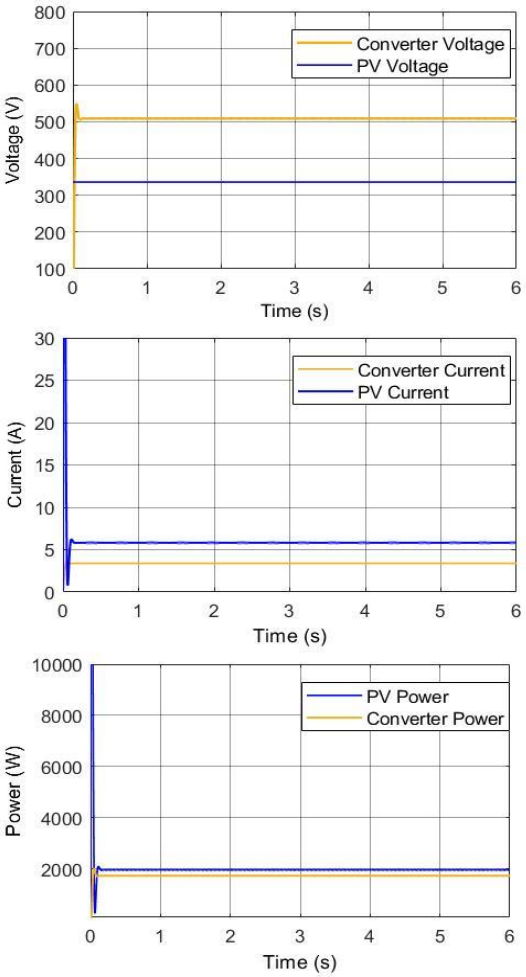

Fig. 17 Boost DC-DC Converter Output Characteristics

The output power is read at 1700 W indicating a 20 W power loss. This loss is also attributed to the reasons mentioned. A duty cycle of 0.35 and a triangular carrier wave of frequency and amplitude 20 kHz and 1 respectively were employed. The ON and OFF duration of the MOSFET were 26 µs and 24 µs. The output current value was 3 A which is relatively close to the 3.44 A calculated. The inductor current also remains above zero ensuring CCM operation. The current and voltage ripples were 0.3 A and 0.5 V respectively, which are within acceptable limits. However, the peak overshoot for the output waveforms were found to be above 50 % whiles the settling time was a little over 1 s. The high overshoots are attributed to the high inductance and capacitance values.

The P & O script was then embedded in a MATLAB user-defined function in Simulink and then connected to the PV array and the boost converter., At STC, the PV produced a maximum power of 1700 W at a voltage of 330 V and current of 5.13 A. Which are close to the desired values of

1720 W, 336 V and 5.13 A. The MPPT started with the initial 0.5 duty cycle and after 0.5 seconds fell to 0.35 after achieving the MPP, the PV current falls from short-circuit current to the MPP current within this time. Also, the boost current rises to the calculated maximum current of 3.44 A similar to illustrations in Fig. 18.

In Fig. 18, the array was exposed to varying irradiance and due to the oscillations of the MPP, the relative change in the duty cycle is not well visualised however, average values and displayed peaks were found to be changing. In this figure, the irradiance was varied between 1000 W/m^2 and 600 W/m^2. The system was connected to 150 Ω load. The voltage and power drops accounted for the losses. At each irradiance, the MPPT produced a corresponding power and voltage – 1700 W, 330 V at 1000 W/m^2 and 980 W, 315 V at 600 W/m^2. The values, amidst some losses, reflect the expected values of 1720 W, 336 V at 1000 W/m^2 and 1057 W, 320 V at 600 W/m^2. With the temperature constant at 25 ℃, the change in current was more significant than that of voltage. Voltage and current varied directly proportional to the change in irradiance. However, the MPPT was slow in response and oscillated at the MPP.

Under constant irradiance and varying temperature, the PV voltage rose from 260 V at 75 °C to 320 V at 50 °C and then to 336 V at 25 °C as indicated in Fig. 19. This is in opposite to the effect of increasing irradiation. The MPP of each operating temperature of PV power rose steadily from 1280 W to 1440 W and then to 1700 W with decreasing temperatures. The MPPT responds relatively faster in this case, but still oscillated. Further, the voltage varied more significantly than current when the irradiance is kept constant.

The entire integrated system was then simulated. Thus, the PV array connected to the MPPT controlled converter and then the inverter. This simulation ran for 6 s at a sampling period of 5 µs, first in steady-state conditions under nominal operating conditions of 25 ºC and 1000 W/m^2 and then under varying atmospheric conditions. Fig. 20 shows the Simulink model of the entire system. The responses are displayed in Fig. 21 and 22. Fig. 21 shows the PV array with the MPPT controlled boost converter responses whiles Fig. 22 displays the inversion side responses in zoomed mode. In the simulation, the system functions without any control for the first 0.5 seconds. After which the MPPT is enabled. The inverter control, however, is enabled after 1.5 s.

PV and boost converter voltages are shown in the first sub-plot with current and power shown in subsequent sub-plots.

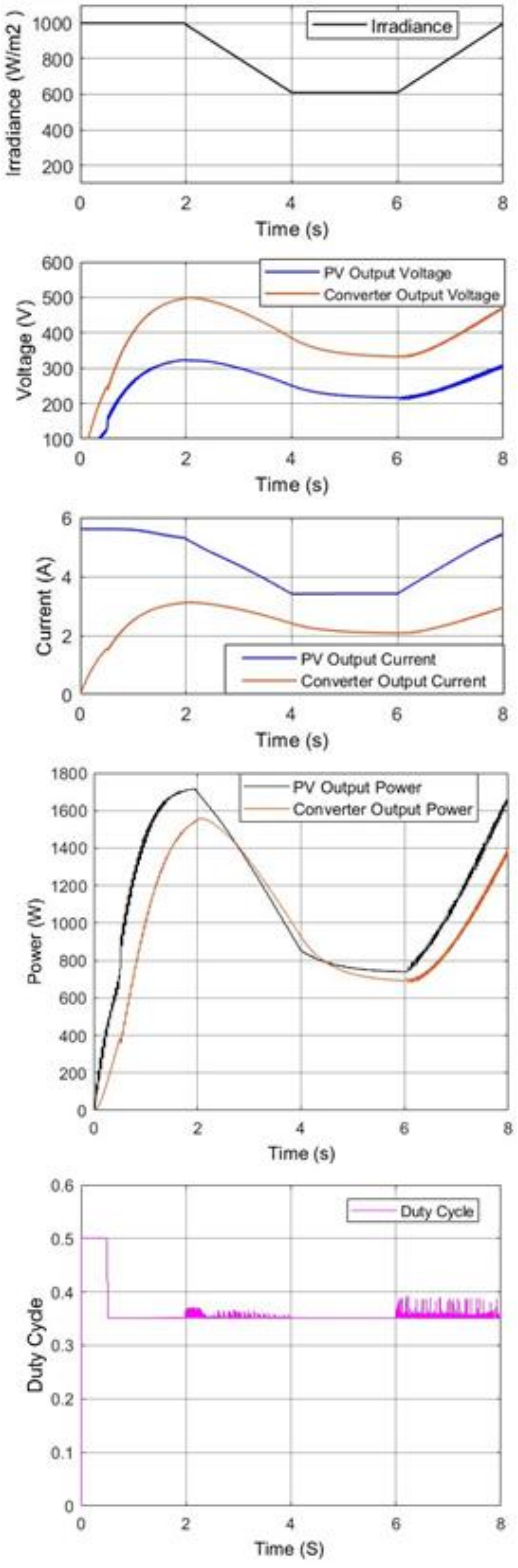

Fig. 18 Output Waveforms of the MPPT Controlled Boost Converter coupled with PV Array at Varying Irradiance Levels

During the first 0.5 s, the boost converter operates with the initial duty ratio of 0.5 and doubles the PV output.

The power rises while current stays at short circuit current. With the

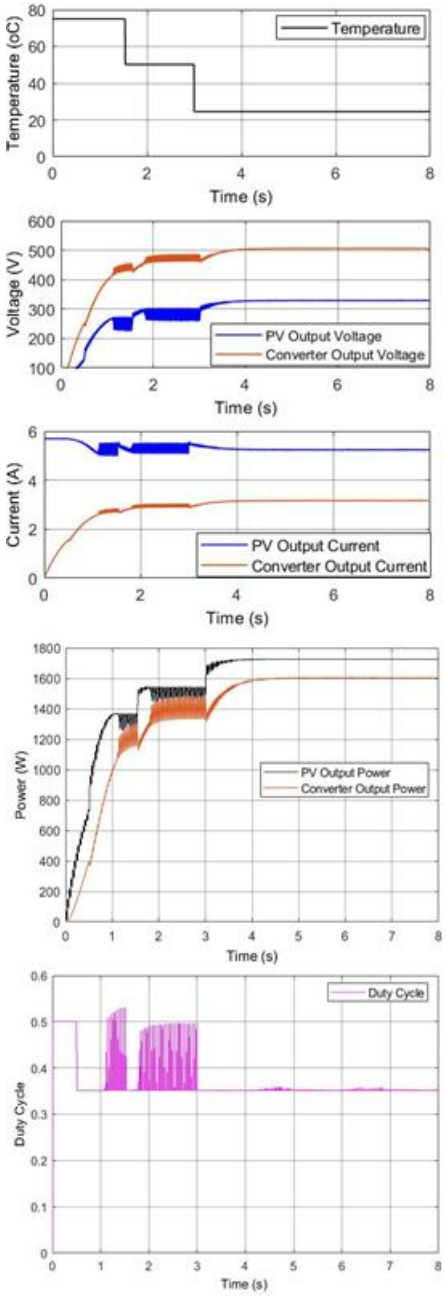

Fig. 19 Output Waveforms of the MPPT Controlled Boost Converter with PV Array at Varying Temperatures

MPPT enabled, both voltages and power increase steadily to the maximum power point of 1700 W, 336 V while PV output current falls to the MPP current of 5.13 A. The duty cycle also dropped to the minimum value as the MPP was achieved. On grid connection, the PV experienced a drastic drop in voltage and power. The current however, declined slightly. The power and current responses also exhibited a high spike upon inverter connection but gained steady state. The voltage responses, however recovered and attempted to reach the MPP with a steady-state loss of 100 V. The drop in voltage and power can be attribute to the load impedances associated with the inverter, LCL filter and the grid. Again, the P&O algorithm fails to function in rapidly changing circumstances and also introduces oscillations into the system. These combined with the low robustness of the algorithm, accounts for the losses, voltage drops and the oscillations in the combined system.

In the Fig. 22 the first and third sub-plots show the grid phase voltage and current respectively. While the second and fourth show the inverter output voltage and current. The grid phase voltage shows a peak of 340 V whiles the inverter voltage has a less 200 V. From the figure, it the evident that the output of the inverter and the grid are in phase. They match in phase and frequency.

The system was then simulated under varying atmospheric conditions. It was exposed to different irradiances and temperatures. The grid and inverter responses are displayed in Fig. 22. Within the first 0.5 seconds, the system runs without any control at nominal conditions. The PV and boost converter voltages and powers begin to rise while the PV output current stays at the short-circuit current. The MPPT is enabled at 0.5 s and at this time the irradiance also begins to drop. The PV current also drops as it varies directly proportional with the irradiance, but the voltage is altered slightly. Power also drops. Between 1 and 1.5 seconds, the irradiance is 200 W/m^2 and temperature is 25 ºC. Current is significantly reduced while voltage is slightly reduced. A lower power value is also attained. From 2 seconds to 5 seconds, the temperature was varied. The variation produces pronounced chances in the voltage more than in the current. During these variations, the P&O was slow in reacting to the changes. Again, upon the connection of the inversion system, the system ripples significantly increased. The ripple content is however, reduced by the LCL filter connected to the output of the inverter. With the inversion side, the voltage and current continued to match the grid phase and frequency. The inverter output voltage maintained a steady-state value irrespective of the variation. The current on the other hand experience little changes.

4 Conclusion

The aim of this project was to evaluate the performance of a three-phase grid connected PV inverter system that utilized the Perturb and Observe algorithm. A 1.7 kW PV inverter system was modeled for grid connection. To achieve this, the project was divided into two major sections. In the first, the Sanyo HIP-215NKHE5 solar module was simulated at different temperature and irradiance conditions and the model displayed

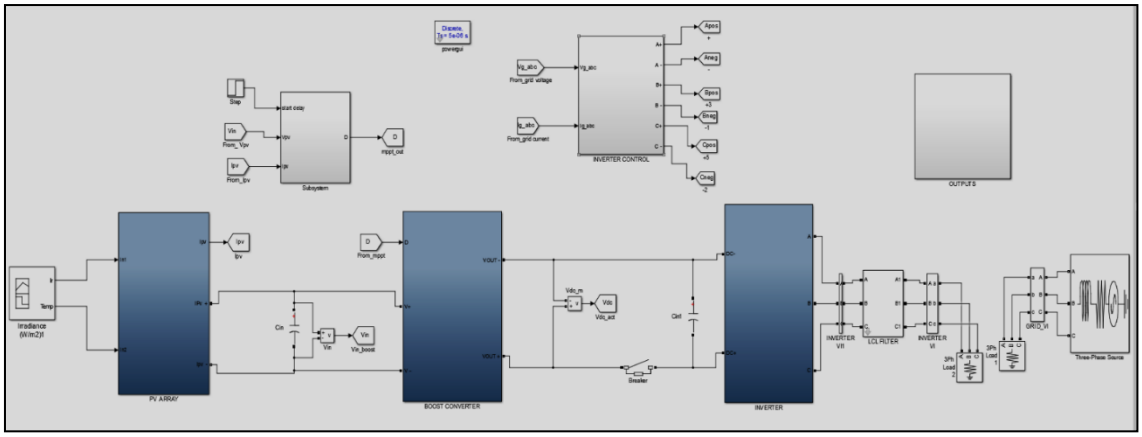

Fig. 20 Simulink Model of Grid-Connected PV Inverter Control System

characteristics that matched the manufacturer's specifications. An array of 8 series connected cell was simulated to provide a higher voltage need for grid integration. The total power from the array was 1720 W at a voltage of 336 V at standard conditions. Also, a boost DC-DC converter controlled by the P&O algorithm was modeled and simulated. The boost converter stepped up the PV output voltage and it operation were enhance by the MPPT algorithm.

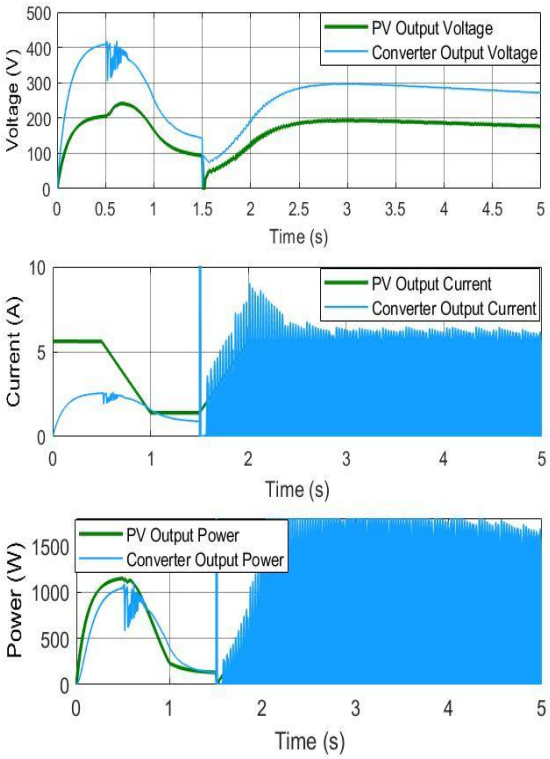

Fig. 21 Output Waveforms of Boost Converter of Entire Integrated System

With the MPPT enabled, maximum power was obtained from panel at all conditions. The second section was the inverter system. The inverter was a three-phase inverter modeled to provide 1.7 kW.

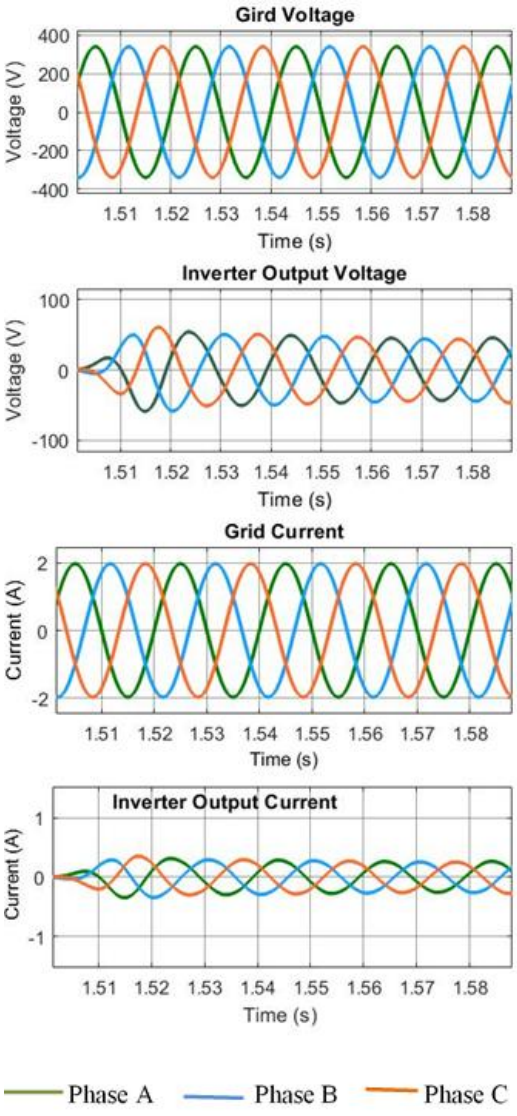

Fig. 22 Output Waveforms of PV Inverter Control System

An LCL filter was used with the inverter to filter out the higher frequency components in the inverter output. A cascaded voltage-current loop control was employed. This control involved the use of

PLL for grid synchronization and the d-q reference frame control. The overall system operated at 75 % efficiency. The change to irradiance was more pronounced in current readings while that of temperature affected the voltage output. The LCL filter also accounted for some losses in the system. However, with this control, reactive power is controlled, and DC link voltage is maintained irrespective of the changing PV voltages.

References

Abdalrahman, A., Zekry, A. and Alshazly, A. (2012), "Simulation and Implementation of Grid-Connected Inverters", *International Journal of Computer Applications*, Vol .60, No.4, pp. 41–49.

Altin, N. and Ozdemir, S. (2013), "Three-Phase Three-Level Grid Interactive Inverter with Fuzzy Logic Based Maximum Power Point Tracking Controller", *Journal of Energy Conversion and Management*. Vol. 69 (2013), pp. 17-26.

Anon. (2009), "Sanyo HIT Photovoltaic Module Datasheet", *Sanyo Component Europe GmbH*, 2 pp.

Cespedes, M. and Sun, J. (2014), "Adaptive Control Of Grid-Connected Inverters Based On Online Grid Impedance Measurements", *IEEE Trans-actions on Sustainable Energy*. IEEE, Vol. 5, No. 2, pp. 516–523.

Chan, P. W. and Masri, S. (2010), "DC-DC Boost Converter with Constant Output Voltage for Grid Connected Photovoltaic Application System", 2010 *International Conference on Intelligent and Advanced Systems*, Manila, Philippines, pp. 1-4.

Das, D. and Pradhan, S. K. P. (2011), "Modeling and Simulation of PV Array With Boost Converter : An Open Loop Study", *Unpublished B. Tech. Project Report*, National Institute of Technology, Rourkela, 47 pp.

Faisal, S.M. A. (2012), "Model of Grid-Connected Photovoltaic System Using MATLAB / SIMULINK", *International Journal of Electrical Engineering*, Vol. 12, pp. 173 -184.

Hannan, M. A., Zambre, A. G., Mohammed, A., and Uddin, M. N. (2015), "Real-Time Testing of A Fuzzy Logic Controller Based Grid Connected Photovoltaic Inverter System", *IEEE Transactions on Industry Applications*, Vol. 51, No. 1, pp. 4775 – 4784.

Hasaneen, B. M. and Mohammed, A. A. E. (2008), "Design and Simulation of DC/DC Boost Cconverter", *2008 12th International Middle East Power System Conference, MEPCON 2008*, Aswan, Egypt, pp. 335 – 340.

Jia, Y., Zhao, J. and Fu, X. (2014), "Direct Grid Current Control of LCL -Filtered Grid-Connected Inverter Mitigating Grid", *IEEE Transactions on Power Electronics*, Vol. 29, No. 3, pp. 1532–1541.

Kammoun, S., Sallem, S. and Kammoun, M. B. A. (2014), "Fuzzy Maximum Power Extraction Control for a Photovoltaic Water Pumping System", *International Journal of Energy Technology and Policy*, Vol. 10, No. 2, pp. 161–181.

Makhlouf, M., Messai, F., Nabti, K. and Benalla, H. (2012), "Modeling and Simulation of Grid-Connected Photovoltaic Distributed Generation System", *2012 1st International Conference on Renewable Energies and Vehicular Technology, REVET 2012*, Hammamet, pp. 187–193.

Mohan, N., Undeland, T. M. and Robbins, W. P. (1995), *Power Electronics -Converters, Applications and Design*, John Wiley and Sons Inc., Canada, 2nd edition, 821 pp.

Mooniarsih, N. T., Syafrudin, M., Mohd, H. and Ayong, H. (2018), "A Grid-Connected Photovoltaic Interface System for Delivering Active and Reactive Powers", *International Journal of Power Electronics and Drive Systems (IJPEDS)*, Vol. 9, No. 3, pp. 1140 - 1146.

Nandurkar, M. S. R. and Rajeev, M. M. (2012), "Design and Simulation of Three Phase Inverter for Grid Connected Photovoltic Systems", *Third Biennial National Conference on Nascent Technologies in the Engineering*, Navi Mumbai, India, pp. 80 - 83.

Nzar, S. P. M. (2014), "Single Phase Grid Connected Photovoltaic System Utilsing Maximum Power Point Tracking", *Unpublished MSc Thesis Work* Newcastle University, 84 pp.

Pandiarajan, N. and Muthu, R. (2011), "Mathematical Modeling of Photovoltaic Module with Simulink", *2011 1st International Conference on Electrical Energy Systems, ICEES 2011*, Newport Beach, USA, pp. 258–263.

Pattanaik, P. A., Pilli, N. K. and Singh, S. K. (2016), "Design, Simulation & Performance Evaluation of Three Phase Grid Connected PV Panel", *2015 IEEE Power, Communication and Information Technology Conference, PCITC 2015*, Bhubaneswar, India, pp. 195–200.

Truong, V. A. and Tho, T. Q. (2013), "Three-Phase Grid-Connected Inverter Using Current Regulator", *International Journal of Electrical Engineering & Technology*, Vol. 4, No. 2 pp. 293–304.

Authors

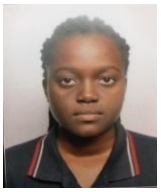

A. B. Asiedu-Asante is an Assistant Lecturer currently working in the Department of Electrical and Electronic Engineering of the Unversity of Mines and Technology, (UMaT) Tarkwa, Ghana. She holds the degrees of BSc in Electrical and Electronic Engineering from UMaT, and MSc in Automation and Control from Newcastle University, UK. She is a member of IEEE. Her

research interests are in instrumentation, automation, and control, process control and hybrid renewable energy systems and power electronics.

R. A. Ofosu is a Lecturer in the Electrical and Electronic Engineering Department at the University of Mines and Technology (UMaT), Tarkwa, Ghana. He holds the degrees of BSc (Electrical and Electronic Engineering) from UMaT and MSc (Electrical and Electronic Engineering) from JKUAT, Kenya. He is a member of the Institute of Electrical and Electronic Engineers (IEEE). His research interests include control engineering, industrial automation, embedded systems, electrical machines and drives, artifical intelligence, frequency control of power system and electrical cable tension control.